Gravitational and Tectonic Stresses in Anisotropic Rock with Irregular Topography

E. PAN†
B. AMADEI†
W. Z. SAVAGE‡

An analytical method is presented to predict stresses in rock masses with smooth and irregular topographies formed by the superposition of multiple long and symmetric ridges and valleys. The rock masses are subject to gravity, uniaxial tectonic horizontal compression or tension acting normal to the ridge and valley axis, or to combined gravitational and tectonic loadings. The method can be applied to ridges and valleys of realistic shape, in generally anisotropic, orthotropic, transversely isotropic, or nearly isotropic rock masses. Numerical examples are presented to show the nature of the in situ stress field in transversely isotropic rock masses with different symmetric and asymmetric topographies under gravitational loading, uniaxial tectonic horizontal loading, or combined gravitational and tectonic loading. Under gravity alone, it is shown that non-zero horizontal compressive stresses exceeding the vertical stress develop at and near ridge crests, and that horizontal tensile stresses develop under isolated valleys. Addition of a horizontal uniaxial compression to gravity increases slightly the horizontal compression at the crest of ridges and diminishes the horizontal tension in valley bottoms. Addition of the horizontal tectonic stress has little effect on the magnitude of the vertical stress.

INTRODUCTION

The effect of surface topography on gravitational stresses has been addressed in the past using two types of analytical methods. One is the exact conformal mapping method, as presented by Akhpatelov and Ter-Martirosyan [1], Ter-Martirosyan and Akhpatelov [2], Ter-Martirosyan *et al.* [3], and Savage *et al.* [4]. However, this approach is restricted to isotropic media, to smooth topographic profiles for which conformal mapping functions can be found exactly, and to two-dimensional problems. The other approach for two- and three-dimensional problems in isotropic media is the perturbation method discussed by McTigue and Mei [5,6] and Liu and Zoback [7]. Liao *et al.* [8] also used the perturbation method for two dimensional problems in anisotropic media. In general, the perturbation method can handle any smooth topographic feature but is restricted to topographies with small slopes not exceeding 10%.

The topographic effect on regional tilt, strain and tectonic stresses has been addressed in the past using the finite element method [9], the perturbation method [5, 10, 11] and the exact conformal mapping method [12].

All the solutions derived with the exact conformal mapping and perturbation methods show clearly that topography can have a major effect on the magnitude and distribution of stresses *in situ*. For instance, the expressions in Savage *et al.* [4] for gravitational stresses in long symmetric isotropic ridges and valleys clearly depend on the geometry of the topography as well as the Poisson's ratio for the rocks. It was found (1) that non-zero horizontal compressive stresses exceeding the vertical stress develop at and near ridge crests and (2) that horizontal tensile stresses develop under valleys. The horizontal compressive stresses in ridge crests decrease and the horizontal tensile stresses in valleys become more compressive with increasing Poisson's ratio. As shown by Savage and Swolfs [12], superposing on the gravitational stresses the effect of a uniaxial tectonic compression acting normal to the axial planes of isolated symmetric ridges and valleys results in a slight increase in the lateral component of the compressive stresses at the ridge crests. Under the valley bottoms, this

†Department of Civil Engineering, University of Colorado, Boulder, CO 80309-0428, U.S.A.
‡U.S. Geological Survey, Box 25046, MS 966, Denver CO 80225, U.S.A.

superposition results in a decrease in the tensile stresses. The opposite effects occur when a far-field tectonic tension is superposed on the gravitational stress field.

In a recent paper, Pan and Amadei [13] presented a new analytical method for determining the stress field in a homogeneous, general anisotropic and elastic half space subject to gravity and surface loads under a condition of generalized plane strain and limited by irregular (but smooth) outer boundaries. Expressions for the stresses in an anisotropic half space with an irregular outer boundary were derived. The stresses were found to depend on three analytical functions that can be determined using a numerical conformal mapping method and an integral equation method. This solution was used more recently by the authors to determine gravity-induced stresses in long *symmetric* transversely isotropic ridges and valleys with planes of anisotropy striking parallel to the ridge or valley axis [14]. Parametric studies were presented on the effect of (1) topography, (2) orientation of anisotropy, and (3) degree of anisotropy on the magnitude and distribution of gravitational stresses.

In this paper, we now consider the topographic modification of tectonic stresses in the absence or presence of gravity. This is done for generally anisotropic, orthotropic, transversely isotropic, or nearly isotropic rock masses modeled as linearly elastic continua with smooth and *asymmetric* topographies constructed by the superposition of multiple long and symmetric ridges and valleys. Numerical examples are presented to show the nature of the *in situ* stress field in transversely isotropic rock masses with different symmetric and asymmetric topographies under gravitational loading, uniaxial tectonic horizontal loading, or combined gravitational and tectonic loading. Finally, a discussion of the implications of the solutions to the understanding of crustal *in situ* stresses is given.

STATEMENT OF THE PROBLEM

Consider the equilibrium of an anisotropic half space with the geometry of Fig. 1. The half space represents a rock mass with an irregular topography. The medium in
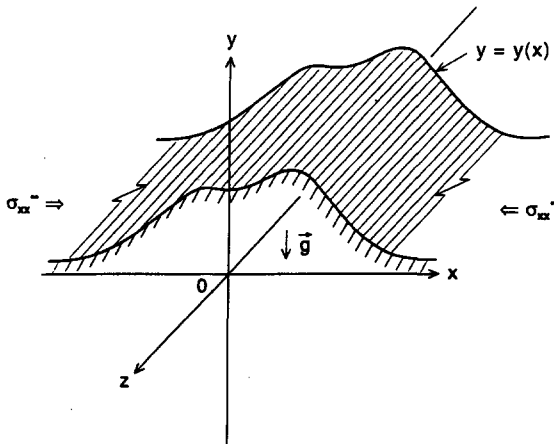
Fig. 1. Half space limited by a boundary curve $y = y(x)$, and subject to gravity, g, and a far-field horizontal and uniform tectonic stress σ_{xx}^{∞}.

the half space is assumed to be linearly elastic, homogeneous, anisotropic and continuous with a uniform density ρ. An x, y, z coordinate system is attached to the half space so that the x and z axes are in the horizontal plane and the y axis points upward. The half-space geometry and the medium's elastic properties are assumed to be independent of the z direction. The boundary curve of the half space is defined by an analytic function $y = y(x)$ or in parametric form $x = x(t)$, $y = y(t)$. The half space is subject to gravity, g, acting in the $-y$ direction and a far-field horizontal and uniform tectonic stress, σ_{xx}^{∞}, acting in the x direction.

The problem is to find the magnitude and distribution of the stresses induced by gravitational and/or tectonic loading of the half space. As done by Pan et al. [14] for symmetric ridges and valleys under gravity only, the stresses are determined assuming a condition of generalized plane strain [15]. In general, the stresses and strains in the x, y, z coordinate system, induced by gravitational and tectonic loading satisfy several basic equations [13]: (1) equations of equilibrium, (2) compatibility conditions and (3) boundary conditions. Furthermore, the six strain components $[e] = [\epsilon_x \epsilon_y \epsilon_z \gamma_{yz} \gamma_{xz} \gamma_{xy}]^T$ are related to the six stress components $[\sigma] = [\sigma_x \sigma_y \sigma_z \tau_{yz} \tau_{xz} \tau_{xy}]^T$ through constitutive relations expressed as follows

$$[e] = [a][\sigma] \tag{1}$$

where [a] is a 6×6 symmetric compliance matrix with 21 independent components $a_{ij}(i, j = 1-6)$. As in Pan et al. [14], the rock mechanics sign convention that compressive stresses are positive is adopted.

ANALYTICAL SOLUTION OF THE PROBLEM

Adding the tectonic stress σ_{xx}^{∞} to the stresses obtained from the gravitational solution of Pan et al. [14] gives the following expression for the six stress components in the half space of Fig. 1

$$\sigma_{xx} = 2\text{Re}[\mu_1^2 \Phi_1'(z_1) + \mu_2^2 \Phi_2'(z_2) + \mu_3^2 \lambda_3 \Phi_3'(z_3)]$$
$$+ c_1 \rho g y - \sigma_{xx}^{\infty}$$

$$\sigma_{yy} = 2\text{Re}[\Phi_1'(z_1) + \Phi_2'(z_2) + \lambda_3 \Phi_3'(z_3)] + \rho g y$$

$$\sigma_{xy} = -2\text{Re}[\mu_1 \Phi_1'(z_1) + \mu_2 \Phi_2'(z_2) + \mu_3 \lambda_3 \Phi_3'(z_3)]$$

$$\sigma_{xz} = 2\text{Re}[\mu_1 \lambda_1 \Phi_1'(z_1) + \mu_2 \lambda_2 \Phi_2'(z_2) + \mu_3 \Phi_3'(z_3)] + c_2 \rho g y$$

$$\sigma_{yz} = -2\text{Re}[\lambda_1 \Phi_1'(z_1) + \lambda_2 \Phi_2'(z_2) + \Phi_3'(z_3)]$$

$$\sigma_{zz} = -\frac{2}{a_{33}}\text{Re}\{[a_{13}\mu_1^2 + a_{23} - a_{34}\lambda_1$$
$$+ a_{35}\mu_1\lambda_1 - a_{36}\mu_1]\Phi_1'(z_1) + [a_{13}\mu_2^2 + a_{23} - a_{34}\lambda_2$$
$$+ a_{35}\mu_2\lambda_2 - a_{36}\mu_2]\Phi_2'(z_2) + [a_{13}\lambda_3\mu_3^2 + a_{23}\lambda_3 - a_{34}$$
$$+ a_{35}\mu_3 - a_{36}\mu_3\lambda_3]\Phi_3'(z_3)\}$$
$$+ c_3 \rho g y. \tag{2}$$

In equation (2), $c_k(k = 1, 2, 3)$, $\mu_k(k = 1, 2, 3)$ and $\lambda_k(k = 1, 2, 3)$ have the same significance as in Pan et al. [14]. Also, $\Phi_k'(z_k)(k = 1, 2, 3)$ denote the derivatives of three analytical functions $\Phi_k(z_k)$ with respect to the

variable $z_k = x + \mu_k y$, where x and y are the coordinates of the point in the anisotropic medium at which the stresses are calculated. The three functions $\Phi_k(z_k)$ must satisfy the traction-free boundary conditions along the boundary curve $y = y(x)$ which can be expressed as follows

$$2\text{Re}[\Phi_1(z_1) + \Phi_2(z_2) + \lambda_3\Phi_3(z_3)]$$

$$= -\rho g \int_0^s yx'(s)\,ds \quad (3)$$

$$2\text{Re}[\mu_1\Phi_1(z_1) + \mu_2\Phi_2(z_2) + \mu_3\lambda_3\Phi_3(z_3)]$$

$$= \int_0^s [\sigma_{xx}^\infty - c_1\rho gy]y'(s)\,ds \quad (4)$$

$$2\text{Re}[\lambda_1\Phi_1(z_1) + \lambda_2\Phi_2(z_2) + \Phi_3(z_3)]$$

$$= -c_2\rho g \int_0^s yy'(s)\,ds \quad (5)$$

where s is the arc-length along the curve $y = y(x)$. There, $x'(s)$ and $y'(s)$ are the total derivatives of x and y with respect to s, respectively.

The determination of the three functions $\Phi_k(z_k)$ and their derivatives depends mainly upon the geometry of the boundary curve $y = y(x)$. As shown by Pan and Amadei [13], these functions can be determined using a numerical conformal mapping method [16] and an integral equation method [17]. Three new analytical functions $\Psi_k (k = 1, 2, 3)$ are introduced such that

$$\Psi_k'(\zeta_k) = \Phi_k'(z_k)Z_k'(\zeta_k) \quad (k = 1, 2, 3) \quad (6)$$

where $z_k = Z_k(\zeta_k)(k = 1, 2, 3)$ are three conformal mapping functions that map the lower half planes bounded by $z_k = x(t) + \mu_k y(t)$ onto the lower flat half planes $\text{Im }\zeta_k \leqslant 0$ $(k = 1, 2, 3)$. This is done in three steps [13]. First, the lower half planes bounded by $z_k = x(t) + \mu_k y(t)$ are mapped onto irregular bounded domains w_k. Then, the domains w_k are mapped onto unit disks F_k. Finally, the unit disks F_k are mapped onto the flat half planes ζ_k. In equation (6), $\Psi_k'(\zeta_k)$ and $Z_k'(\zeta_k)$ are the total derivatives of Ψ_k and Z_k with respect to ζ_k. As shown by Pan and Amadei [13], if t_k is the value of ζ_k on the boundary curve, the boundary conditions (3)–(5) lead to the following system of three singular integral equations that can be solved for the three functions $\Psi_k'(t_k)$

$$b_{11}\Psi_1'(\tau_1) + \frac{b_{12}}{2}\Psi_2'(\tau_2)t_2'(\tau_1) + \frac{b_{13}}{2}\Psi_3'(\tau_3)t_3'(\tau_1)$$

$$+ \frac{b_{12}}{2\pi i} \int_{+\infty}^{-\infty} \frac{\Psi_2'(t_2)t_2'(t_1)\,dt_1}{t_1 - \tau_1}$$

$$+ \frac{b_{13}}{2\pi i} \int_{+\infty}^{-\infty} \frac{\Psi_3'(t_3)t_3'(t_1)\,dt_1}{t_1 - \tau_1}$$

$$= \frac{f_1(\tau)t'(\tau_1)}{2} + \frac{1}{2\pi i} \int_{+\infty}^{-\infty} \frac{f_1(t)t'(t_1)\,dt_1}{t_1 - \tau_1} \quad (7)$$

$$b_{21}\Psi_2'(\tau_2) + \frac{b_{22}}{2}\Psi_1'(\tau_1)t_1'(\tau_2) + \frac{b_{23}}{2}\Psi_3'(\tau_3)t_3'(\tau_2)$$

$$+ \frac{b_{22}}{2\pi i} \int_{+\infty}^{-\infty} \frac{\Psi_1'(t_1)t_1'(t_2)\,dt_2}{t_2 - \tau_2}$$

$$+ \frac{b_{23}}{2\pi i} \int_{+\infty}^{-\infty} \frac{\Psi_3'(t_3)t_3'(t_2)\,dt_2}{t_2 - \tau_2}$$

$$= \frac{f_2(\tau)t'(\tau_2)}{2} + \frac{1}{2\pi i} \int_{+\infty}^{-\infty} \frac{f_2(t)t'(t_2)\,dt_2}{t_2 - \tau_2} \quad (8)$$

$$b_{31}\Psi_3'(\tau_3) + \frac{b_{32}}{2}\Psi_1'(\tau_1)t_1'(\tau_3) + \frac{b_{33}}{2}\Psi_2'(\tau_2)t_2'(\tau_3)$$

$$+ \frac{b_{32}}{2\pi i} \int_{+\infty}^{-\infty} \frac{\Psi_1'(t_1)t_1'(t_3)\,dt_3}{t_3 - \tau_3}$$

$$+ \frac{b_{33}}{2\pi i} \int_{+\infty}^{-\infty} \frac{\Psi_2'(t_2)t_2'(t_3)\,dt_3}{t_3 - \tau_3}$$

$$= \frac{f_3(\tau)t'(\tau_3)}{2} + \frac{1}{2\pi i} \int_{+\infty}^{-\infty} \frac{f_3(t)t'(t_3)\,dt}{t_3 - \tau_3}. \quad (9)$$

The coefficients $b_{ij}(i, j = 1, 2, 3)$ and the functions $f_i(t)(i = 1, 2, 3)$ in equations (7)–(9) are given by equations (A1) and (A2) in the Appendix of the paper by Pan et al. [14]. The only difference is in the expression of $f_1(t)$, $f_2(t)$ and $f_3(t)$ where $v(t)$ is now equal to $(c_1\rho gy(t) - \sigma_{xx}^\infty)y'(t)$ instead of $c_1\rho gy(t)y'(t)$. In equations (7)–(9), τ is a fixed point on the $t[-\infty, +\infty]$ axis and $\tau_k(k = 1, 2, 3)$ are fixed points on the $t_k(\text{Im }\zeta_k = 0)$ axes. There, $t'(t_j)$ and $t_k'(t_j)(k, j = 1, 2, 3)$ are the total derivatives of t and t_k with respect to the variable $t_j[-\infty, +\infty]$ and are equal to

$$t'(t_j) = \frac{Z_j'(t_j)}{x'(t) + \mu_j y'(t)};$$

$$t_k'(t_j) = \frac{Z_j'(t_j)}{Z_k'(t_k)} \cdot \frac{x'(t) + \mu_k y'(t)}{x'(t) + \mu_j y'(t)} \quad (10)$$

where $x'(t)$ and $y'(t)$ are the total derivatives of x and y with respect to t.

The three integral equations (7)–(9) can be discretized and solved for the boundary values of the three analytical functions $\psi_k'(t_k)$ by the method proposed by Sarkar et al. [18]. Then, the interior values of these analytical functions are calculated using the Cauchy integral theorem [19]. Finally, the stress functions $\Phi_k'(z_k)$ are obtained using equation (6) and the six stress components are determined using equation (2). The infinite integrals appearing in equations (7)–(9) are determined using an inverse mapping from the boundary of the ζ_k planes to the circumference of unit discs. For these integrals to converge, the boundary curve $x = x(t)$, $y = y(t)$ must be asymptotic to the x-axis of Fig. 1 at $x = \pm\infty$.

It can be shown that the six stress components defined in equation (2) satisfy the conditions that shear and normal stresses vanish along the boundary $y = y(x)$. Furthermore, as $x \to \pm\infty$, the stress field approaches the

testonic stress field if only tectonic loading is active. For gravitational loading only, the lateral strains ϵ_x and γ_{xz} approach zero as $x \to \pm\infty$, consistent with the results given by Savage et al. [20] for the isotropic case. The stresses are such that the longitudinal strain ϵ_z is equal to zero for gravitational loading only or to a constant value, $a_{31}\sigma_{xx}^{\infty}$, if tectonic loading is active, where a_{31} is a component for matrix [a] defined in equation (1).

STRESSES BELOW RIDGES AND VALLEYS WITH COMPLEX TOPOGRAPHIES

Generalized plane-strain solution

The topography is assumed to be smooth and to be expressed in parametric form as follows.

$$x(t) = t \quad (-\infty < t < +\infty)$$

$$y(t) = \sum_{i=1}^{N} y_i(t) \tag{11}$$

with

$$y_i(t) = \frac{a_i^2 b_i}{(t - x_i)^2 - a_i^2}. \tag{12}$$

Equations (11) and (12) correspond to the geometric superposition of $i = 1$, N symmetric ridges or valleys $x(t)$, $y_i(t)$ centered at $x = x_i$. If b_i is positive, equation (12) corresponds to a ridge with height b_i. If b_i is negative, equation (12) corresponds to a valley with depth $|b_i|$. The parameter a_i controls the lateral extent of each ridge or valley with inflection points located at $x = x_i \pm a_i/\sqrt{3}$, $y = 0.75b_i$ at which the slopes are equal to $\pm 3b_i\sqrt{3}/(8a_i)$ [14]. Thus, different complex and smooth topographies can be obtained by choosing different positive or negative values of a_i, b_i and x_i for $i = 1$, N. As an example, Figs 2(a) and (b) show asymmetric topographies obtained by superposition of $N = 2$ symmetric ridges or valleys, respectively.

For the topography defined in equations (11) and (12), the mappings $z_k = Z_k(\zeta_k)$ ($k = 1, 2, 3$) which map the lower half planes bounded by $z_k = x(t) + \mu_k y(t)$ onto the flat lower half planes $\text{Im}\,\zeta_k \leq 0$ ($k = 1, 2, 3$) consist of three successive conformal mappings (Fig. 3):

Mapping 1:

$$z_k \Rightarrow w_k \quad k = 1, 2, 3$$

$$w_k(t) = \frac{z_k(t) + iA_k}{z_k(t) - iA_k} \quad -\infty < t < \infty \tag{13}$$

with

$$z_k(t) = t + \mu_k \sum_{i=1}^{N} a_i^2 b_i / [(t - x_i)^2 + a_i^2] \tag{14}$$

maps the lower half planes bounded by $z_k = x(t) + \mu_k y(t)$ onto irregular bounded domains w_k. In equation (13), A_k ($k = 1, 2, 3$) are complex constants chosen such that the mapping is conformal. In equation (13), the variable t can be replaced by a new parameter θ that varies over a finite interval $[-\pi/2, \pi/2]$ such that $t = \tan\theta$. Then equation (13) takes the following form

$$w_k(\theta) = \frac{p(\theta) + iA\cos\theta}{p(\theta) - iA\cos\theta} \quad k = 1, 2, 3; \quad -\frac{\pi}{2} < \theta < \frac{\pi}{2} \tag{15}$$

with

$$p(\theta) = \sin\theta + \mu_k \sum_{i=1}^{N} \frac{a_i^2 b_i \cos^3\theta}{(\sin\theta - x_i\cos\theta)^2 + a_i^2\cos^2\theta}. \tag{16}$$

Mapping 2:

$$w_k \Rightarrow F_k \quad k = 1, 2, 3$$

$$F_k = F_k(w_k) \tag{17}$$

maps the irregular bounded domains w_k onto unit discs F_k. This is done using a numerical conformal mapping method as discussed in Trummer [16] and Pan and Amadei [13].
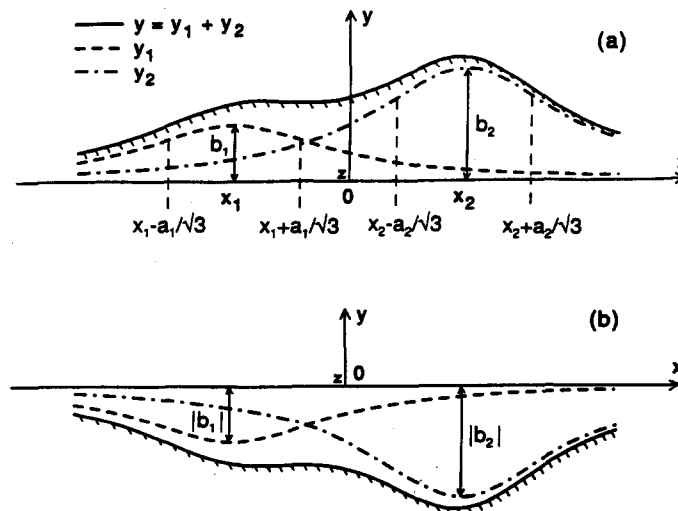

Fig. 2. Asymmetric topographies obtained by superposition (a) of two separate symmetric ridges with $b_1/|b_2| = 0.5$ and $b_2|b_2| = 1$, (b) of two separate symmetric valleys with $b_1/|b_2| = -0.5$ and $b_2/|b_2| = -1$. In (a) and (b) $a_1/|b_2| = 1$, $a_2/|b_2| = 1$, and $x_2/|b_2| = 1$.
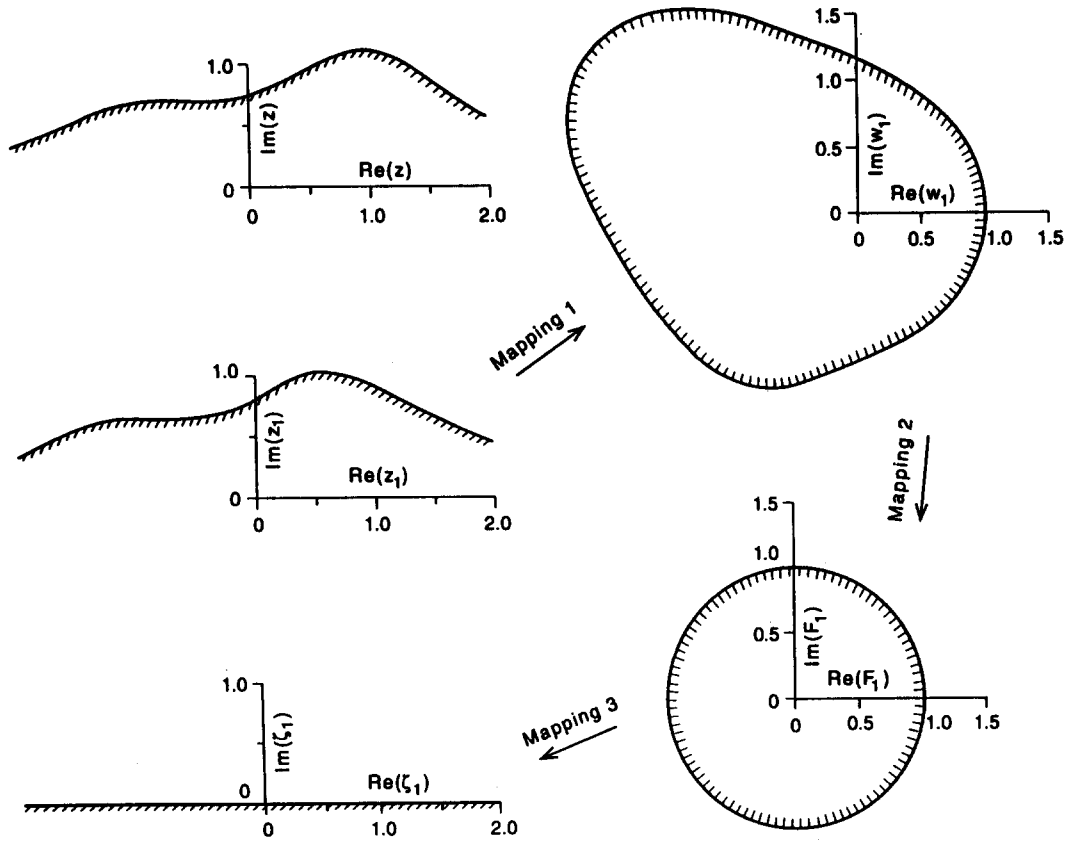
Fig. 3. Example of mappings 1, 2 and 3 for $k = 1$ and the geometry of Fig. 2(a). $E/E' = G/G' = 3$, $v = 0.25$, $v' = 0.15$ and $\psi = 45°$.

Mapping 3:

$$F_k \Rightarrow \zeta_k \quad k = 1, 2, 3$$

$$\zeta_k = i \frac{F_k(w_k) + 1}{F_k(w_k) - 1} \tag{18}$$

maps the unit discs F_k onto the flat half-planes ζ_k.

For the topography defined in equations (11) and (12), $t'(t_j)$ and $t'_k(t_j)$ defined in (10) take the following form

$$t'(t_j) = \frac{Z'_j(t_j)}{1 - 2\mu_j q(t)}$$

$$t'_k(t_j) = \frac{Z'_j(t_j)}{Z'_k(t_k)} \cdot \frac{1 - 2\mu_k q(t)}{1 - 2\mu_j q(t)} \tag{19}$$

with

$$q(t) = \sum_{i=1}^{N} \frac{a_i^2 b_i (t - x_i)}{[(t - x_i)^2 + a_i^2]^2}. \tag{20}$$

The rock mass with the geometry of Fig. 1 is assumed to be *orthotropic* in an n, s, t cartesian coordinate system attached to planes of anisotropy in the medium. The orientation of this coordinate system with respect to the x, y, z coordinate system is defined by a dip azimuth β and a dip angle ψ as shown in Fig. 4. The t-axis is located in the xz plane. The constitutive equation for the

rock in the n, s, t coordinate system is given by the following equation [15]

$$
\begin{bmatrix} \epsilon_n \\ \epsilon_s \\ \epsilon_t \\ \gamma_{st} \\ \gamma_{nt} \\ \gamma_{ns} \end{bmatrix}
=
\begin{bmatrix}
\frac{1}{E_n} & -\frac{v_{sn}}{E_s} & -\frac{v_{tn}}{E_t} & 0 & 0 & 0 \\
-\frac{v_{ns}}{E_n} & \frac{1}{E_s} & -\frac{v_{ts}}{E_t} & 0 & 0 & 0 \\
-\frac{v_{nt}}{E_n} & -\frac{v_{st}}{E_s} & \frac{1}{E_t} & 0 & 0 & 0 \\
0 & 0 & 0 & \frac{1}{G_{st}} & 0 & 0 \\
0 & 0 & 0 & 0 & \frac{1}{G_{nt}} & 0 \\
0 & 0 & 0 & 0 & 0 & \frac{1}{G_{ns}}
\end{bmatrix}
\begin{bmatrix} \sigma_{nn} \\ \sigma_{ss} \\ \sigma_{tt} \\ \sigma_{st} \\ \sigma_{nt} \\ \sigma_{ns} \end{bmatrix}
\tag{21}
$$

or in a more compact matrix form as

$$[\mathbf{e}]_{nst} = [\mathbf{h}] [\mathbf{\sigma}]_{nst}. \tag{22}$$

In equation (21), E_n, E_s and E_t are, respectively, the Young's moduli in the n, s and t directions, respectively. The moduli G_{ns}, G_{nt} and G_{st} are, respectively, the shear moduli in planes parallel to the ns, nt and st planes, respectively. Finally, $v_{ij}(i, j = n, s, t)$ are the Poisson's ratios that characterize the normal strains in the symmetry directions j when a stress is applied in the symmetry directions i. Nine independent elastic constants are needed to describe the deformability of the rock mass in the n, s, t coordinate system.
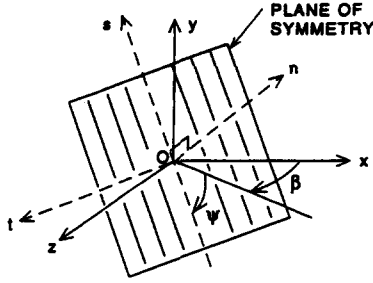
Fig. 4. Orientation of planes of symmetry with respect to the x, y, z coordinate system (after [14]).

If the medium is *transversely isotropic* in one of the three *ns*, *nt* or *st* planes, only five independent elastic constants E, E', v, v' and G' are needed to describe the deformability of the medium in the n, s, t coordinate system where: (i) E and E' are Young's moduli in the plane of transverse isotropy and in a direction normal to it, respectively, (ii) v and v' are Poisson's ratios characterizing the lateral strain response in the plane of transverse isotropy to a stress acting parallel and normal to it, respectively, and (iii) G' is the shear modulus in planes normal to the plane of transverse isotropy.

Because of the linear relationships existing between coefficients a_{ij} and h_{ij} of the matrices [a] and [h] in equations (1) and (22), respectively, it can be shown that, the ratios between the stresses σ_{ij} defined in (2) and a characteristic stress $\rho g |b|$ (where $|b|$ is a characteristic elevation) or the ratios between σ_{ij} and a characteristic stress σ_{xx}^∞ (for tectonic loading only) depend on the following eight dimensionless quantities

$$\frac{E_s}{E_n}; \quad \frac{E_s}{E_t}; \quad v_{sn}; \quad v_{tn}; \quad v_{ts}; \quad \frac{E_s}{G_{st}}; \quad \frac{E_s}{G_{nt}}; \quad \frac{E_s}{G_{ns}}. \quad (23)$$

If the medium is transversely isotropic with, for instance, transverse isotropy in the *st* plane, the stress ratios $\sigma_{ij}/\rho g |b|$ and $\sigma_{ij}/\sigma_{xx}^\infty$ depend only on four dimensionless terms

$$\frac{E}{E'}; \quad v; \quad v'; \quad \frac{G}{G'}. \quad (24)$$

The stress ratios $\sigma_{ij}/\rho g |b|$ and $\sigma_{ij}/\sigma_{xx}^\infty$ also depend on (1) the orientation angles β and ψ of the planes of anisotropy with respect to the x, y and z axes of Fig. 1, (2) the coordinates $(x/|b|, y/|b|)$ of the points at which the stresses are calculated, and (3) the geometry of the topography defined by the ratios $a_i/|b|$, $b_i/|b|$ and $x_i/|b|$ for $i = 1$, N. For combined gravitational and tectonic loading, the stress ratios $\sigma_{ij}/\rho g |b|$ also depend on $\sigma_{xx}^\infty/\rho g |b|$. Equation (2) shows that in general, at each point in the half space, the stress field is three-dimensional and the principal stress components are inclined with respect to the x, y and z axes.

Plane-strain solution

The solution presented above takes a simpler form for orthotropic and transversely isotropic rock masses with planes of elastic symmetry normal to the z axis of Fig. 1. This takes place (1) when the dip azimuth β in Fig. 4 is zero and the dip angle ψ varies between 0 and 90°, or (2)

when β and ψ are equal to 90°. For those cases, the generalized plane-strain solution reduces to a plane-strain solution and the stress components are now equal to

$$\sigma_{xx} = 2\mathrm{Re}[\mu_1^2 \Phi_1'(z_1) + \mu_2^2 \Phi_2'(z_2)] + c_1 \rho g y - \sigma_{xx}^\infty$$

$$\sigma_{yy} = 2\mathrm{Re}[\Phi_1'(z_1) + \Phi_2'(z_2)] + \rho g y$$

$$\sigma_{xy} = -2\mathrm{Re}[\mu_1 \Phi_1'(z_1) + \mu_2 \Phi_2'(z_2)]$$

$$\sigma_{xz} = \sigma_{yz} = 0$$

$$\sigma_{zz} = -\frac{2}{a_{33}} \mathrm{Re}\{[a_{13}\mu_1^2 + a_{23} - a_{36}\mu_1]\Phi_1'(z_1)$$

$$+ [a_{13}\mu_2^2 + a_{23} - a_{36}\mu_2]\Phi_2'(z_2)\} + c_3 \rho g y. \quad (25)$$

Equation (25) shows that at each point beneath the surface, two of the three principal stresses induced by gravity and the far-field tectonic stress are located in the x, y plane and that the longitudinal stress σ_{zz} is the third principal stress.

NUMERICAL EXAMPLES

In the numerical examples presented below, the geometry of Figs 2(a) and (b), and Fig. 4 is adopted. The rock mass is assumed to be either isotropic or transversely isotropic. Note that the anisotropic solution presented in this paper becomes singular if the rock mass is isotropic with $E/E' = G/G' = 1$ and $v = v'$ [13]. This is because the formulation for isotropic elasticity is different from that for anisotropic media as discussed by Lekhnitskii [15]. The isotropic case can, however, be approached asymptotically by considering a nearly isotropic rock with $E/E' = G/G' = 1$, $v = 0.25$ and $v' = 0.24$, *and* $\psi = 0°$.

Figures 5–8 show contours of dimensionless stresses $\sigma_{xx}/\rho g |b|$, $\sigma_{yy}/\rho g |b|$ and $\sigma_{xy}/\rho g |b|$ or $\sigma_{xx}/\sigma_{xx}^\infty$, $\sigma_{yy}/\sigma_{xx}^\infty$ and $\sigma_{xy}/\sigma_{xx}^\infty$ for a symmetric ridge or valley, centered at $x_1 = 0$, with height $b_1 = b$ or depth $|b_1| = |b|$ and $a_1/|b| = 1$. For this geometry, the inflection points of the ridge or valley are located at $x/|b| = \pm\sqrt{3}/3$ and $y/|b| = \pm 0.75$ at which the slopes are equal to $\pm(3\sqrt{3})/8$ (or 33.0°).

Figures 5(a)–(c) are contour diagrams of dimensionless tectonically induced stresses $\sigma_{xx}/\sigma_{xx}^\infty$, $\sigma_{yy}/\sigma_{xx}^\infty$ and $\sigma_{xy}/\sigma_{xx}^\infty$ for a ridge in a nearly isotropic rock mass. Here σ_{xx}^∞, the uniform far-field horizontal tectonic stress, is assumed to be compressive and gravity is not active. Because of symmetry, only the right halves of the plots of stress contours are presented. Note that the signs of $\sigma_{xy}/\sigma_{xx}^\infty$ will be opposite on the left halves. Similar contour diagrams for a symmetric valley are shown in Figs 6(a)–(c). Comparing Figs 5(a) and 6(a), $\sigma_{xx}/\sigma_{xx}^\infty$ is less than unity near the ridge crest and larger than unity and concentrated at the valley bottom. With increasing depth, $\sigma_{xx}/\sigma_{xx}^\infty$ approaches unity under both topographic features. Figs 5(b) and 6(b) show that the dimensionless vertical stress ratio $\sigma_{yy}/\sigma_{xx}^\infty$ is an order of magnitude smaller than $\sigma_{xx}/\sigma_{xx}^\infty$ in both the ridge and valley. Also, concentrations of $\sigma_{xy}/\sigma_{xx}^\infty$ develop on the flanks of the ridge and valley.
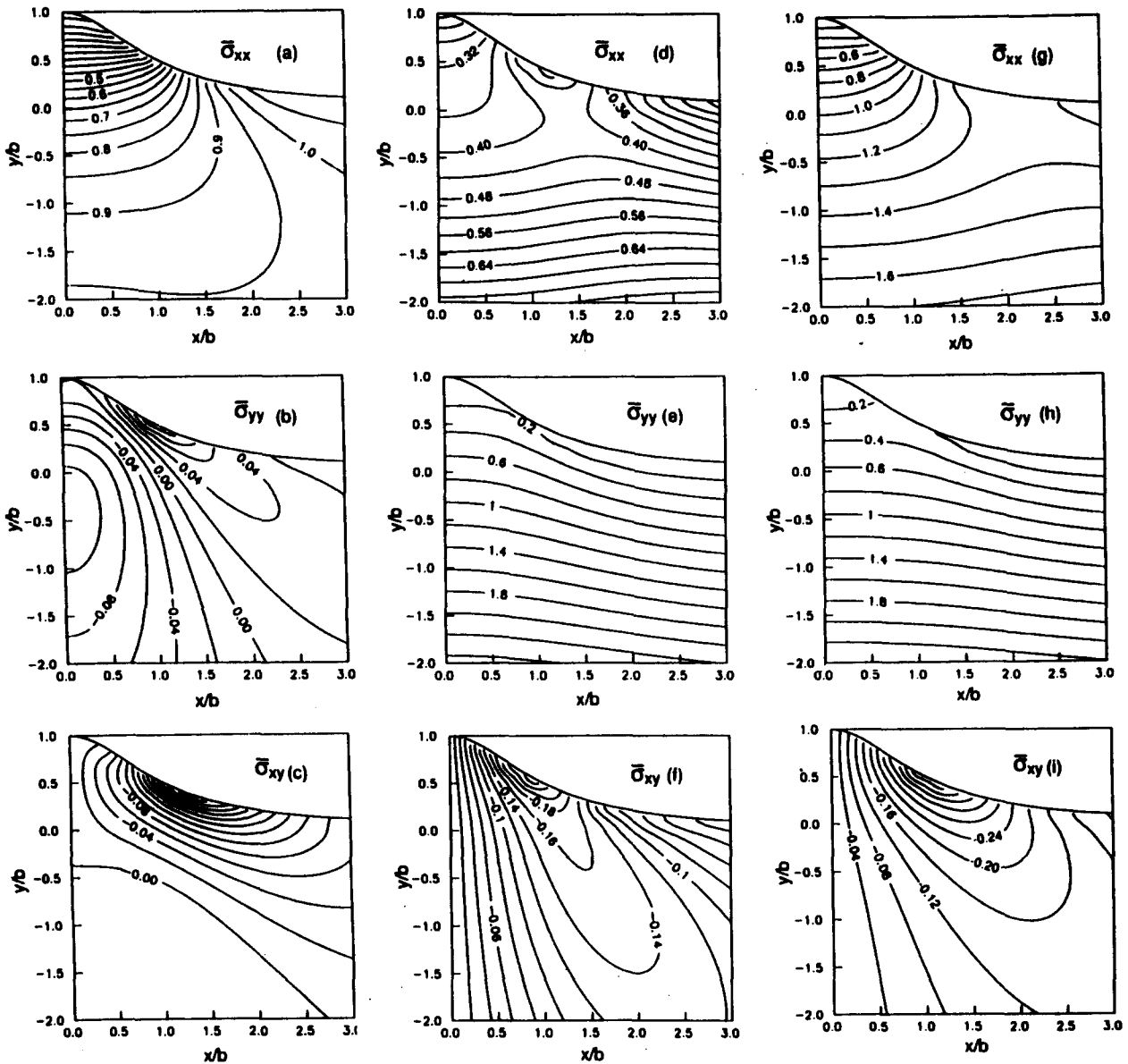
Fig. 5. Stress contour diagrams for a symmetric ridge with $a_1/|b| = 1$ in a nearly isotropic rock mass ($E/E' = G/G' = 1$, $v = 0.25$, $v' = 0.24$ and $\psi = 0°$). Contour diagrams of $\sigma_{xx}/\sigma_{xx}^\infty$, $\sigma_{yy}/\sigma_{xx}^\infty$ and $\sigma_{xy}/\sigma_{xx}^\infty$ in (a), (b) and (c), respectively, for tectonic loading only. Contour diagrams of $\sigma_{xx}/\rho g |b|$, $\sigma_{yy}/\rho g |b|$ and $\sigma_{xy}/\rho g |b|$ in (d), (e) and (f), respectively, for gravitational loading only. Contour diagrams of $\sigma_{xx}/\rho g |b|$, $\sigma_{yy}/\rho g |b|$ and $\sigma_{xy}/\rho g |b|$, respectively, in (g), (h) and (i) induced by gravity and a far-field tectonic stress $\sigma_{xx}^\infty = \rho g |b|$. The dimensionless stresses are defined as $\bar{\sigma}_{xx}$, $\bar{\sigma}_{yy}$, and $\bar{\sigma}_{xy}$.

For comparison, Figs 5(d)–(f) and Figs 6(d)–(f) are, respectively, contour diagrams of dimensionless gravity-induced stresses $\sigma_{xx}/\rho g |b|$, $\sigma_{yy}/\rho g |b|$ and $\sigma_{xy}/\rho g |b|$ for a ridge and a valley in a nearly isotropic rock mass subject to gravity only. Figures 5(d) and 6(d) indicate a concentration of compressive stress $\sigma_{xx}/\rho g |b|$ on the sides of the ridge and tensile stress $\sigma_{xx}/\rho g |b|$ at the valley bottom. For the ridge and the valley, the contours of $\sigma_{yy}/\rho g |b|$ nearly follow the ridge and valley shape [Figs 5(e) and 6(e)]. Also, concentrations of $\sigma_{xy}/\rho g |b|$ can be seen on the lower sides of the ridge and valley in Figs 5(f) and 6(f), respectively.

The combined effect of gravitational and horizontal tectonic loading on the stresses in the ridge and valley in a nearly isotropic rock mass is illustrated in Figs 5(g)–(i) and Figs 6(g)–(i). In this example, the uniform far-field horizontal tectonic stress σ_{xx}^∞ is assumed to be compres-

sive and equal to the characteristic stress $\rho g |b|$. Comparing Figs 5(d)–(f) with Figs 5(g)–(i) for a ridge and Figs 6(d)–6(f) with Figs 6(g)–(i) for a valley, indicates that addition of a far-field horizontal tectonic stress $\rho g |b|$ increases the magnitude of $\sigma_{xy}/\rho g |b|$ and, to a greater extent, the magnitude of the horizontal stress $\sigma_{xx}/\rho g |b|$. However, under the crest of the ridge only a slight increase in compressive stress $\sigma_{xx}/\rho g |b|$ occurs; for instance from 0.31 to 0.66 at $x/|b| = 0$ and $y/|b| = 0.5$. Also, the concentration of $\sigma_{xx}/\rho g |b|$ on the sides of the ridge in Fig. 5(d) disappears in Fig. 5(g). At the valley bottom, addition of the tectonic stress changes the sign of $\sigma_{xx}/\rho g |b|$ from tensile to compressive; for instance from -0.98 to 2.72 at $x/|b| = 0$ and $y/|b| = -1.0$. In general, with increasing depth, σ_{xx} increases by $\rho g |b|$. The results shown in Figs 5 and 6 are essentially identical to those obtained by Savage

et al. [4] and Savage and Swolfs [12] for symmetric ridges and valleys in isotropic rock but with slightly different geometries.

The effect of anisotropy on the stress distribution in a symmetric ridge and valley is shown in Figs 7 and 8. The rock mass is transversely isotropic with planes of transverse isotropy parallel to the z-axis of Fig. 4 ($\beta = 0°$) and is such that $E/E' = G/G' = 3$, $v = 0.25$, and $v' = 0.15$. It is subject to combined gravitational loading and a horizontal far-field tectonic stress σ_{xx}^{∞} equal to $\rho g |b|$.

Figures 7(a)–(c) show contour diagrams of $\sigma_{xx}/\rho g |b|$, $\sigma_{yy}/\rho g |b|$ and $\sigma_{xy}/\rho g |b|$ for a ridge with horizontal planes of transverse isotropy ($\psi = 0°$), and Figs 7(c)–(f) show the corresponding stress contour diagrams for a ridge with vertical planes of transverse isotropy ($\psi = 90°$). Comparing Figs 5(g)–(i) and Figs 7(a)–(f)

reveals similar patterns for the stress contour diagrams for both isotropic and anisotropic rocks. However, the stresses differ in magnitude everywhere except near the crest of the ridge. For instance, at a given point in the ridge, the magnitude of $\sigma_{xx}/\rho g |b|$ is largest in the ridge with horizontal planes of transverse isotropy [Fig. 7(a)], smallest in the ridge with vertical planes of transverse isotropy [Fig. 7(d)], and in between these two extremes for the nearly isotropic case [Fig. 5(g)]. The magnitude of the concentration in $\sigma_{xy}/\rho g |b|$ on the flanks of the ridge is 0.39 for vertical anisotropy [Fig. 7(f)], 0.42 for horizontal anisotropy [Fig. 7(c)], and 0.48 for the nearly isotropic case [Fig. 5(i)]. The magnitude of the vertical stress $\sigma_{yy}/\rho g |b|$ is only slightly affected by the isotropic or anisotropic character of the rock.

Figures 8(a)–(c) show contour diagrams of $\sigma_{xx}/\rho g |b|$, $\sigma_{yy}/\rho g |b|$ and $\sigma_{xy}/\rho g |b|$ for a valley with horizontal
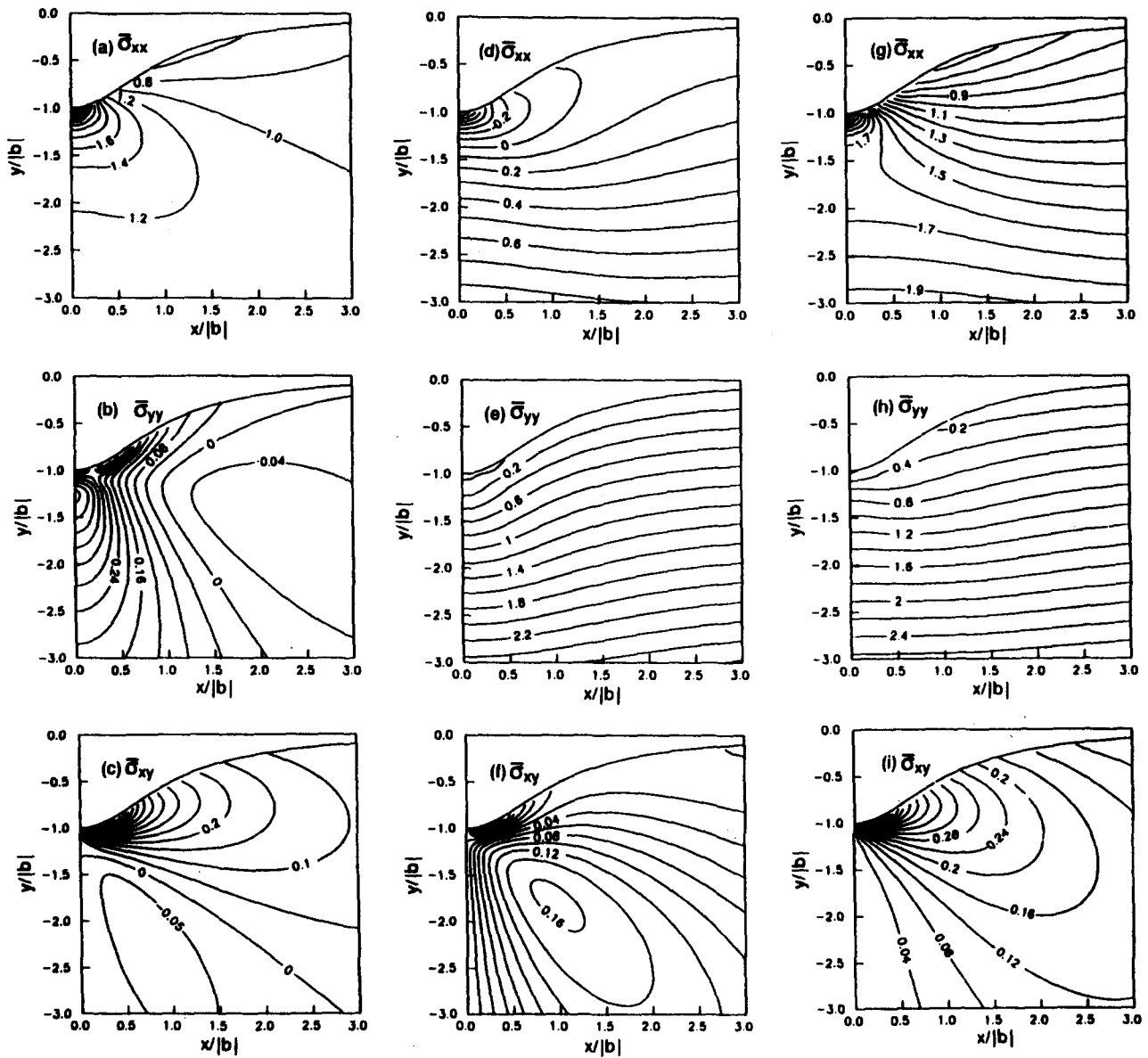

Fig. 6. Stress contour diagrams for a symmetric valley with $a_1/|b| = 1$ in a nearly isotropic rock mass ($E/E' = G/G' = 1$, $v = 0.25$, $v' = 0.24$ and $\psi = 0°$). Contour diagrams of $\sigma_{xx}/\sigma_{xx}^{\infty}$, $\sigma_{yy}/\sigma_{xx}^{\infty}$ and $\sigma_{xy}/\sigma_{xx}^{\infty}$ in (a), (b) and (c), respectively, for tectonic loading only. Contour diagrams of $\sigma_{xx}/\rho g |b|$, $\sigma_{yy}/\rho g |b|$ and $\sigma_{xy}/\rho g |b|$ in (d), (e) and (f), respectively, for gravitational loading only. Contour diagrams of $\sigma_{xx}/\rho g |b|$, $\sigma_{yy}/\rho g |b|$ and $\sigma_{xy}/\rho g |b|$, respectively, in (g), (h) and (i) induced by gravity and a far-field tectonic stress $\sigma_{xx}^{\infty} = \rho g |b|$. The dimensionless stresses are defined as $\bar{\sigma}_{xx}$, $\bar{\sigma}_{yy}$, and $\bar{\sigma}_{xy}$.
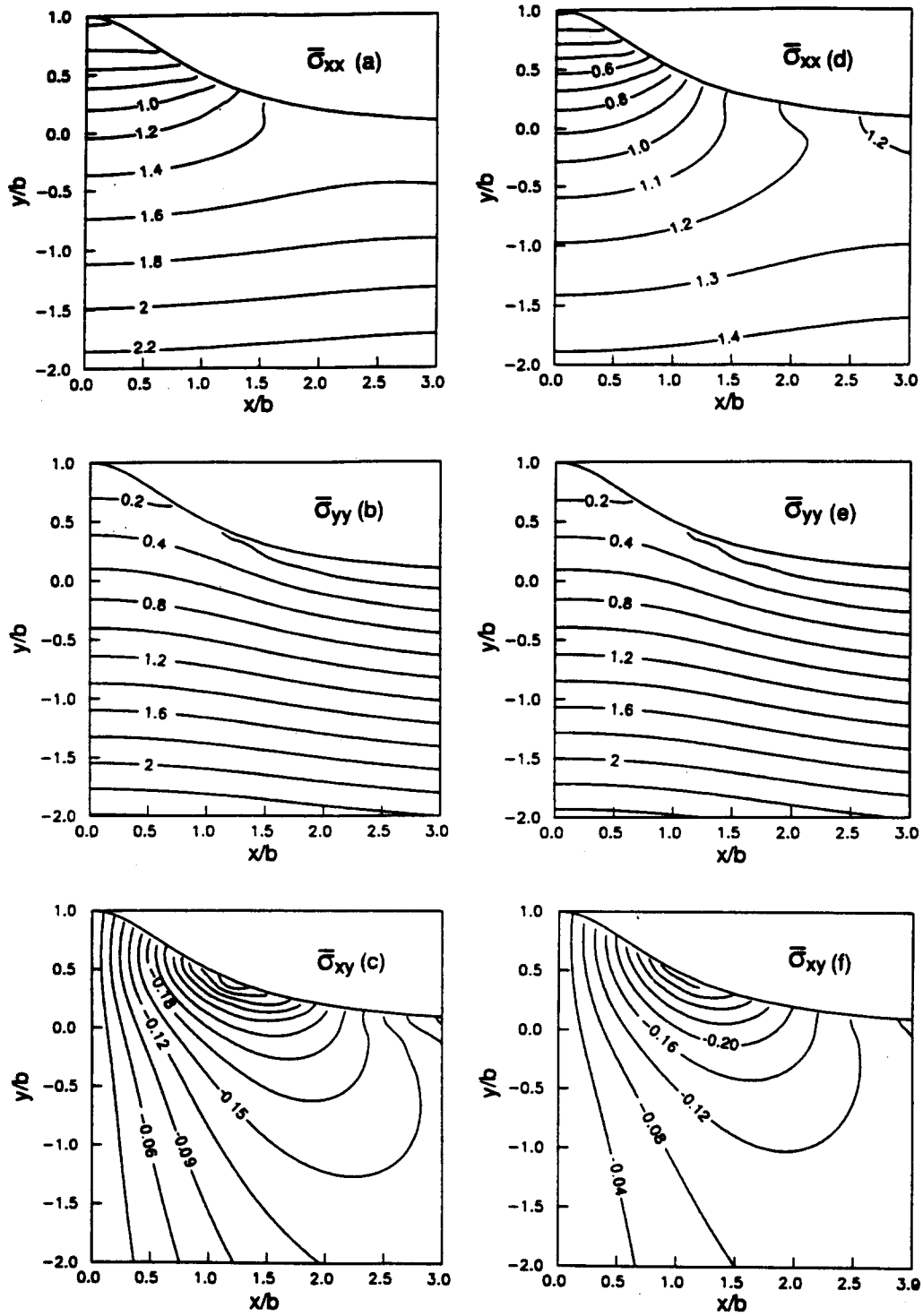
Fig. 7. Contour diagrams of $\bar{\sigma}_{xx} = \sigma_{xx}/\rho g\,|b|$, $\bar{\sigma}_{yy} = \sigma_{yy}/\rho g\,|b|$ and $\bar{\sigma}_{xy} = \sigma_{xy}/\rho g\,|b|$ for a symmetric ridge with $a_1/|b| = 1$ in a transversely isotropic rock mass $(E/E' = G/G' = 3$, $v = 0.25$, $v' = 0.15)$ with horizontal planes of transverse isotropy in (a), (b) and (c), respectively, and vertical planes of transverse isotropy in (d), (e) and (f), respectively. Combined gravitational and tectonic loading with $\sigma_{xx}^{\infty} = \rho g\,|b|$.

planes of transverse isotropy, and Figs 8(d)–(f) show the corresponding stress contour diagrams for a valley with vertical planes of transverse isotropy. As for the ridge, comparing Figs 6(g)–(i) and Figs 8(a)–(f) reveals similar patterns for the stress contour diagrams for both isotropic and anisotropic rocks but differences in the stress magnitudes. For instance, at the valley bottom $(x/|b| = 0$ and $y/|b| = -1.0)$, the concentration of $\sigma_{xx}/\rho g\,|b|$ is 4.1 for horizontal anisotropy [Fig. 8(a)], 2.9 for vertical anisotropy [Fig. 8(d)], and 2.7 for the nearly isotropic case [Fig. 6(g)]. The concentration of $\sigma_{xy}/\rho g\,|b|$ near the bottom of the valley is 0.73 for horizontal anisotropy [Fig. 8(c)], 0.77 for vertical anisotropy [Fig. 8(f)], and 0.74 for the nearly isotropic case [Fig. 6(i)]. Again, the magnitude of the vertical stress $\sigma_{yy}/\rho g\,|b|$ is only slightly affected by the isotropic or anisotropic character of the rock.

As a final numerical example, Figs 9(a)–(f) show stress contour diagrams below a complex (asymmetric) topography similar to that analyzed by Swolfs and Savage [21]. Here, $y(0)$ is the characteristic height equal to elevation of the topography at $x = 0$. The rock is transversely isotropic with planes of transverse isotropy striking parallel to the z-axis of Fig. 4 ($\beta = 0°$) and dipping at an angle $\psi = 30°$ in the $+x$ direction. The

rock-mass elastic properties are such that $E/E' = 2$, $G/G' = 1$ and $v = v' = 0.25$.

Figures 9(a)–(c) show contour diagrams of $\sigma_{xx}/\rho g y(0)$, $\sigma_{yy}/\rho g y(0)$, and $\sigma_{xy}/\rho g(0)$ when the rock mass is subject to gravity only. For comparison, Figs 9(d)–(f) show the corresponding stress contour diagrams when the rock mass is now subject to combined gravitational loading and far-field horizontal tectonic loading
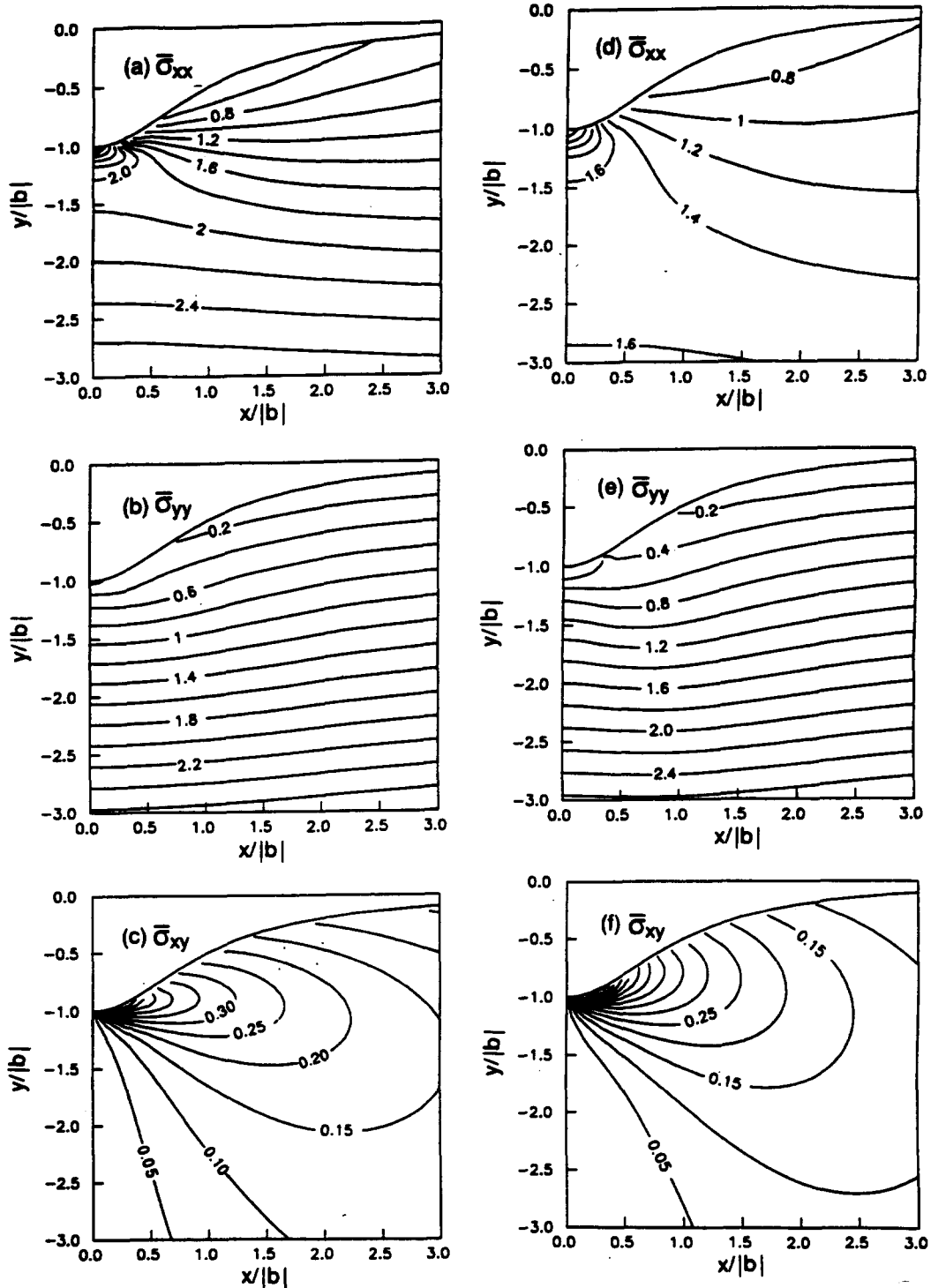

Fig. 8. Contour diagrams of $\bar{\sigma}_{xx} = \sigma_{xx}/\rho g\,|b|$, $\bar{\sigma}_{yy} = \sigma_{yy}/\rho g\,|b|$ and $\bar{\sigma}_{xy} = \sigma_{xy}/\rho g\,|b|$ for a symmetric valley with $a_1/|b| = 1$ in a transversely isotropic rock mass ($E/E' = G/G' = 3$, $v = 0.25$, $v' = 0.15$) with horizontal planes of transverse isotropy in (a), (b) and (c), respectively, and vertical planes of transverse isotropy in (d), (e) and (f), respectively. Combined gravitational and tectonic loading with $\sigma_{xx}^{\infty} = \rho g\,|b|$.

$\sigma_{xx}^{\infty} = \rho g y(0)$. The contours of $\sigma_{yy}/\rho g y(0)$ nearly follow the ridge and valley shape [Figs 9(b) and (e)]. Also, concentrations of compressive stress $\sigma_{xx}/\rho g y(0)$ and shear stress $\sigma_{xy}/\rho g y(0)$ can be seen in the valley at $x/y(0) = 1.6$ in Figs 9(a), (c), (d) and (f). Comparing Figs 9(a)–(c) with Figs 9(d)–(f) shows that addition of a far-field horizontal tectonic stress $\rho g y(0)$ increases the magnitude of $\sigma_{xy}/\rho g y(0)$ near the ground surface and to a greater extent, increases the magnitude of the horizontal stress $\sigma_{xx}/\rho g |b|$. For instance at $x/y(0) = 1.6$. The magnitude of the concentration of $\sigma_{xx}/\rho g y(0)$ is about 0.86 under gravity alone and is 2.5 if tectonic loading is added. Also, addition of the far-field horizontal tectonic stress has little effect on the magnitude of the vertical stress $\sigma_{yy}/\rho g y(0)$ [Figs 9(a) and (e)].
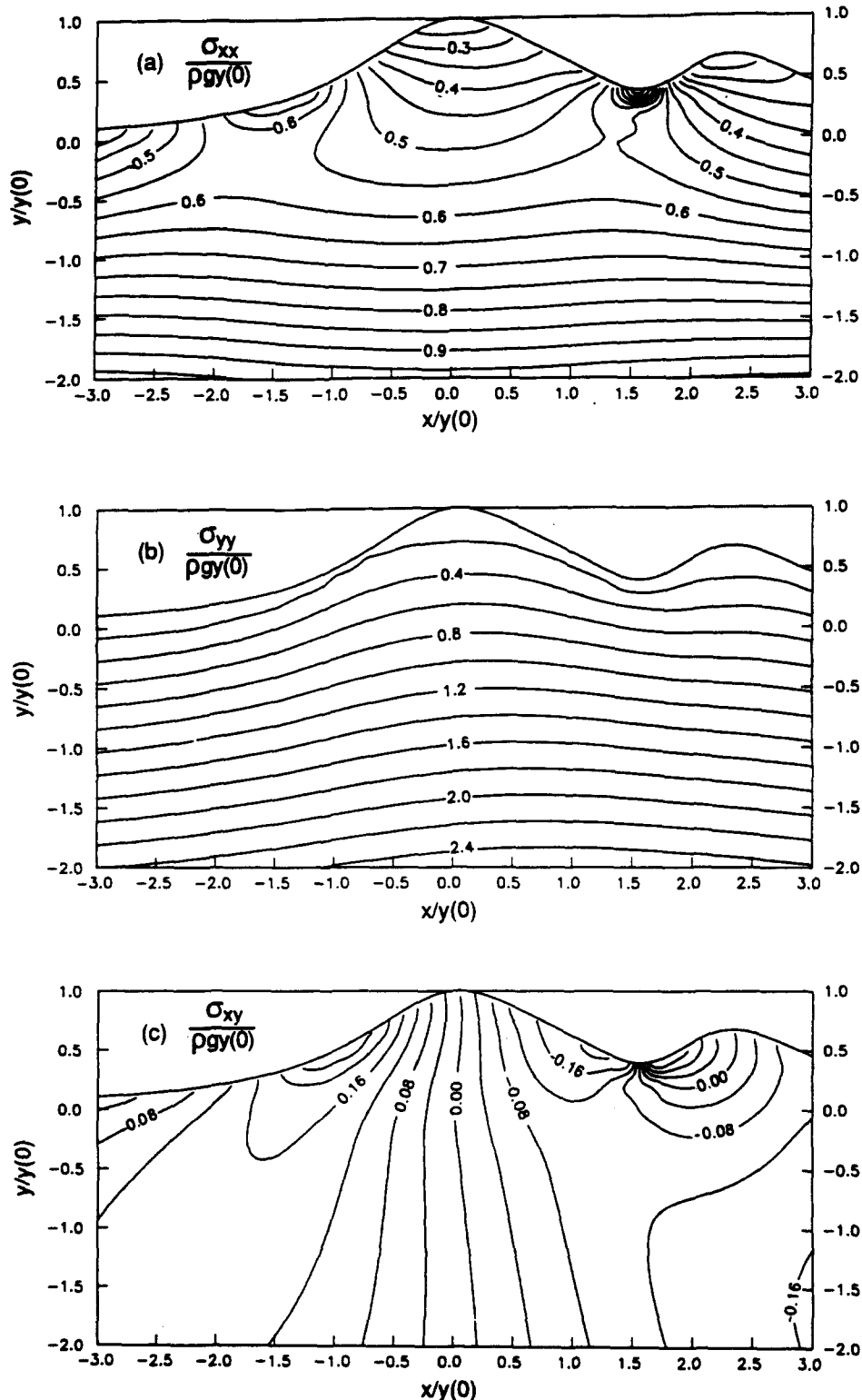
Figs 9 (a–c). *See caption overleaf.*
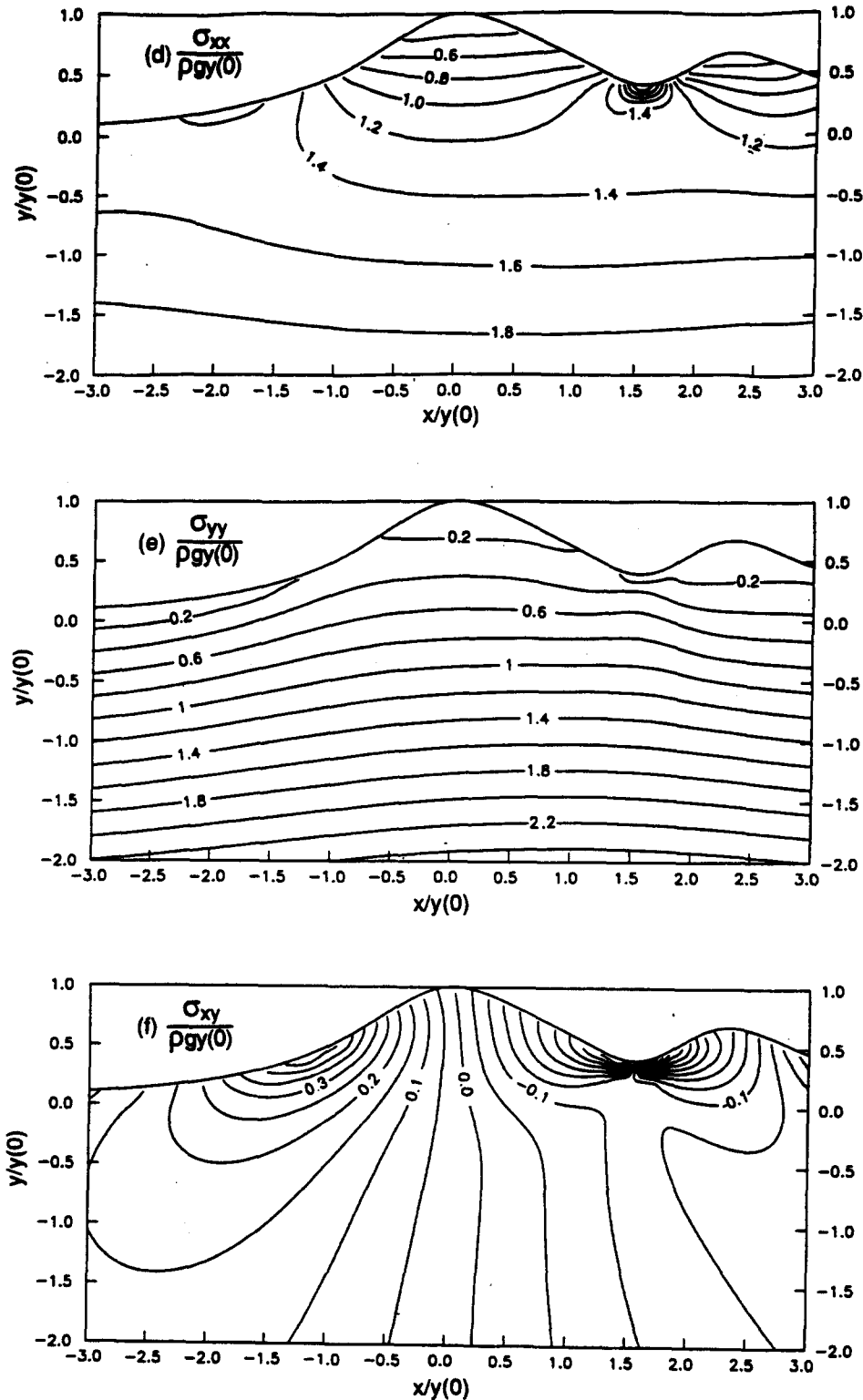
Figs 9 (d–f).

Fig. 9. Contour diagrams of $\sigma_{xx}/\rho gy(0)$, $\sigma_{yy}/\rho gy(0)$ and $\sigma_{xy}/\rho gy(0)$ in a transversely isotropic rock mass ($E/E' = 2$, $G/G' = 1$, $v = v' = 0.25$, $\beta = 0°$ and $\psi = 30°$) under gravity only in (a), (b) and (c), respectively, and under combined gravitational and tectonic loading with $\sigma_{xx}^{\infty} = \rho g |b|$ in (d), (e) and (f), respectively. Topography obtained by superposition of $N = 4$ ridges and valleys with $a_i/y(0) = 1$ for $i = 1–4$, $b_1/y(0) = 0.8983$, $b_2/y(0) = 1.2657$, $b_3/y(0) = -2.1186$, $b_4/y(0) = 1.3438$, $x_1/y(0) = 0$, $x_2/y(0) = 1.35$, $x_3/y(0) = 1.6$, $x_4/y(0) = 2.1$.

DISCUSSION

The state of stress in the Earth's crust has been investigated by a variety of measuring techniques and

predicted by a number of analytical models [20, 22–24]. From *in situ* stress measurements at shallow depths, two common features have been observed [22]: The first is the ubiquity of high horizontal stresses relative to the

overburden-caused vertical stress. The second is that, in many cases, the vertical stress component is not a principal stress. The topographic effect, first proposed by Savage et al. [4] for isotropic rock masses in symmetric ridges and valleys, and extended recently by the authors [13,14] to anisotropic rock masses below any smooth topographies, can give a satisfactory explanation of both observations. For instance, numerical examples in Savage et al. [4], Savage and Swolfs [12], Pan et al. [14] and in this paper all show that the near-surface horizontal stress σ_{xx} in symmetric or asymmetric ridges is non-zero and its value can be high relative to the vertical stress component σ_{yy}, whether the rock mass is nearly isotropic or anisotropic. Even if the ground surface is flat, the horizontal stress can still be higher than the vertical stress because of the effect of anisotropy [25,26]. Furthermore, principal stress trajectories in Pan et al. [14] show clearly that near the surface, the vertical stress component σ_{yy} is not a principal stress except for points along the center line of the symmetric ridge or valley. The same result is shown for the isotropic case by Savage et al. [4].

There is some field evidence for the theoretically predicted tensile stresses near valley bottoms. For instance, Knill [27] found that there is commonly a zone near the valley surface in which the rock mass is loose and discontinuous. Because of this, Knill [27] suggested that underground excavation, tunnelling, or dam foundation should be carried well below this zone. Other evidence for valley bottom tensile stress is rebound near valley bottoms and valley walls as noted by Matheson and Thomson [28]. This upwarping phenomenon may be a consequence of tensile stresses [28–30]. Also, far-field strains or tectonic loading can change the features of the gravity-induced stress field. For example, we have shown in this paper, as did Savage et al. [4], that addition of an initial horizontal uniaxial compression to gravity loading can diminish the horizontal tension, eventually changing it to horizontal compression in valley bottoms.

The results presented above also have implication to earthquake-related problems. For example, to study the state of stress in a mountainous region, Swolfs and Savage [31] approximated the surface topography by a long symmetric ridge. The rock mass in the ridge was assumed to be isotropic and both gravitational and tectonic stresses were calculated from their exact solution. Swolfs and Savage [31] found that the maximum stress differences $\sigma_1 - \sigma_3$ are generally greater in the axial portion of the ridge than beneath its flanks. Thus, gravity and tectonic stress fields are modified by topography to localize and enhance the stress conditions that favor recurrent faulting and seismicity along the axial portion of mountain ranges. An example is the Hida Range, Japan where earthquake swarms occurred in the axial portion of the range [31]. However, if the topography can not be approximated by a long symmetric ridge or the rock mass is anisotropic, the above observation of the location of the maximum stress difference $\sigma_1 - \sigma_3$ may not be true. In order to solve such a complex problem, the present analytical method can be used.

An interesting study would be to compare the analytically predicted stress field in a region with the measured stress field. If the predicted gravity-induced stress field is consistent with the measured field, then one could conclude that the measured stresses are predominantly of gravitational origin. Examples are Fifth Water Ridge, Utah and Yucca Mountain, Nevada as demonstrated by Swolfs and Savage [31]. Otherwise, the region may be subject to tectonic loading, as well as gravity loading. An example is the Hida Range, Japan [31].

CONCLUSION

In this paper, an analytical method is presented to predict stresses in rock masses with smooth topographies constructed by the superposition of multiple long and symmetric ridges and valleys. The method overcomes the small slope topography limitation associated with the perturbation method and the isotropic limitation associated with the exact conformal mapping methods. The rock masses are subject to gravity, uniaxial tectonic horizontal compression or tension acting normal to the ridge and valley axis, or to combined gravitational and tectonic loading. The method, which is an extension of that initially proposed by Pan et al. [14] for gravitational loading of isolated symmetric ridges and valleys, can be applied to ridges and valleys of realistic shapes, in generally anisotropic, orthotropic, transversely isotropic, or nearly isotropic rock masses. It is found that at each point of such rock masses, the stress field is three-dimensional and the principal stresses are inclined with respect to the plane normal to the ridge or valley axis when the planes of anisotropy are inclined with respect to the ridge or valley axis. On the other hand, for rock masses with planes of transverse isotropy parallel to or normal to the valley or ridge axis, two of the three principal stresses are in the plane normal to that axis and the third principal stress is parallel to that axis.

The magnitude of the predicted stresses is on the order of a characteristic stress, $\rho g |b|$, where ρ is the rock density, g is the gravitational acceleration and $|b|$ is a characteristic topographic elevation. Under the effect of a uniaxial tectonic stress, σ_{xx}^{∞}, and in the absence of gravity, the magnitude of the predicted stresses is on the order of σ_{xx}^{∞}. The magnitude and distribution of the stress ratios $\sigma_{ij}/\rho g |b|$ or $\sigma_{ij}/\sigma_{xx}^{\infty}$ depend on (1) the topographic geometry defined by the ratios $a_i/|b|$, $b_i/|b|$ and the location $x_i/|b|$ of the $i = 1, N$ symmetric ridges and valleys comprising the topography, (2) the orientation of the anisotropy with respect to the ridge and valley axis defined by the strike and dip angles of the planes of rock anisotropy, and (3) the degree of rock anisotropy defined by ratios of elastic constants such as E/E', G/G', v and v' for transversely isotropic rocks. For combined gravitational and tectonic loading, the stress ratios $\sigma_{ij}/\rho g |b|$ also depend on $\sigma_{xx}^{\infty}/\rho g |b|$.

As originally shown by Savage and Swolfs [12] and as we show here for symmetric and isotropic ridges and valleys, far-field horizontal tectonic compressions are reduced at ridge crests and concentrated at valley

bottoms. Also, addition of a far-field horizontal uniaxial compression to gravity increases slightly the horizontal compression at the crests of ridges and diminishes the horizontal tension in valley bottoms. Addition of the far-field tectonic stress has little effect on the magnitude of the vertical stress.

For rock masses with identical topographies subject to gravitational and far-field compression, similar patterns in the stress contour diagrams can be observed for both isotropic and anisotropic rocks; however, the stresses differ in magnitude. At a given point in a ridge, the horizontal compression is the largest when the rock is transversely isotropic with horizontal anisotropy, the smallest when the anisotropy is vertical, and in between these two extremes when the rock is isotropic. For a valley, the horizontal compression at the valley bottom is larger for horizontal anisotropy than for vertical anisotropy. The magnitude of the vertical stress is only slightly affected by the isotropic or anisotropic character of the rock.

For more complex topographies, the effect of adding a far-field horizontal compressive stress is, to a great extent, to increase the magnitude of the horizontal stress component near the ground surface. With increasing depth, the horizontal stress increases by the magnitude of the tectonic stress.

The numerical examples presented in this paper are only a sample of possible case studies that can be addressed with our analytical method because it is now possible to consider different topographies of more realistic shapes, rock anisotropy, and the separate or combined effect of gravity and tectonic stresses when estimating the magnitude and distribution of stresses *in situ*.

REFERENCES

1. Akhpatelov D. M. and Ter-Martirosyan Z. G. The stressed state of ponderable semi-infinite domains. *Armenian Acad. Sci. Mech. Bull.* **24**, 33–40 (1971).
2. Ter-Martirosyan Z. G. and Akhpatelov D. M. The stressed state of an infinite slope with a curvilinear boundary subject to a field of gravity and percolation. *J. Probl. Geomech.* **5**, 81–91 (1972).
3. Ter-Martirosyan Z. G., Akhpatelov D. M. and Manvelyan R. G. The stressed state of rock masses in a field body forces. *Proc. 3rd. ISRM Congress*, Denver, part A, 569–574 (1974).
4. Savage W. Z., Swolfs H. S. and Powers P. S. Gravitational stress in long symmetric ridges and valleys. *Int. J. Rock Mech. Min. Sci. & Geomech. Abstr.* **22**, 291–302 (1985).
5. McTigue D. F. and Mei C. C. Gravity induced stresses near topography of small slopes. *J. Geophys. Res.* **86**, 9268–9278 (1981).
6. McTigue D. F. and Mei C. C. Gravity induced stresses near axisymmetric topography of small slopes. *Int. J. Num. Anal. Methods Geomech.* **11**, 257–268 (1987).
7. Liu L. and Zoback M. D. The effect of topography on the state of stress in the crust: Application to the site of the Cajon Pass Scientific Drilling Project. *J. Geophys. Res.* **97**, 5095–5108 (1992).
8. Liao J. J., Savage W. Z. and Amadei B. Gravitational stresses in anisotropic ridges and valleys with small slopes. *J. Geophys. Res.* **97**, 3325–3336 (1992).
9. Harrison J. C. Gravity and topographic effects in tilt and strain measurement. *J. Geophys. Res.* **81**, 319–328 (1976).
10. McTigue D. F. and Stein R. S. Topographic amplification of tectonic displacement: Implications for geodetic measurement of strain changes. *J. Geophys. Res.* **89**, 1123–1131 (1984).
11. Meertens C. M. and Wahr J. M. Topographic effect on tilt, strain, and displacement measurements. *J. Geophys. Res.* **91**, 14,057–14,062 (1986).
12. Savage W. Z. and Swolfs H. S. Tectonic and gravitational stress in long symmetric ridges and valleys. *J. Geophys. Res.* **91**, 3677–3685 (1986).
13. Pan E. and Amadei B. Stresses in an anisotropic rock mass with irregular topography. *J. Eng. Mech.*, *ASCE* **120**, 97–119 (1994).
14. Pan E., Amadei B. and Savage W. Z. Gravitational stresses in long symmetric ridges and valleys in anisotropic rock. *Int. J. Rock Mech. Min. Sci. & Geomech. Abstr.* **31**, 293–312 (1994).
15. Lekhnitskii S. G. *Theory of Elasticity of an Anisotropic Elastic Body*. Holden–Day, San Francisco (1963).
16. Trummer M. R. An efficient implementation of a conformal mapping method based on the Szegö kernel. *SIAM J. Numer. Anal.* **23**, 853–872 (1986).
17. Muskhelishvili N. I. *Singular Integral Equations*. Noordhoff, Groningen, Holland (1972).
18. Sarkar T. K., Yang X. and Arvas E. A limited survey of various conjugate gradient methods for solving complex matrix equations arising in electromagnetic wave interactions. *Wave Motion* **10**, 527–546 (1988).
19. Muskhelishvili N. I. *Some Basic Problems of the Mathematical Theory of Elasticity*. Noordhoof, Groningen, Holland (1953).
20. Savage W. Z., Swolfs H. S. and Amadei B. On the state of stress in the near-surface of the Earth's crust. *PAGEOPH* **138**, 207–228 (1992).
21. Swolfs H. S. and Savage W. Z. Topography, stresses, and stability at Yucca Mountain, Nevada. *Proc. 26th U.S. Symp. Rock Mech.* 1121–1129 (1985).
22. McGarr A. and Gay N. C. State of stress in the Earth's crust. *Ann. Rev. Earth Planet. Sci.* **6**, 405–436 (1978).
23. Gough D. I. and Gough W. I. Stress near the surface of the Earth. *Ann. Rev. Earth Planet. Sci.* **15**, 545–566 (1987).
24. McGarr A. On the state of lithospheric stress in the absence of applied tectonic forces. *J. Geophys. Res.* **93**, 13,609–13,617 (1988).
25. Amadei B. and Pan E. Gravitational stresses in anisotropic rock masses with inclined strata. *Int. J. Rock Mech. Min. Sci. & Geomech. Abstr.* **29**, 225–236 (1992).
26. Amadei B., Savage W. Z. and Swolfs H. S. Gravitational stresses in anisotropic rock masses. *Int. J. Rock Mech. Min. Sci. & Geomech. Abstr.* **24**, 5–14 (1987).
27. Knill J. L. Geotechnical significance of some glacially induced rock discontinuities. *Bull. Assoc. Eng. Geol.* **5**, 49–62 (1968).
28. Matheson D. S. and Thomson S. Geological implications of valley rebound. *Can. J. Earth Sci.* **10**, 961–978 (1973).
29. Silvestri V. and Tabib C. Exact determination of gravity stresses in finite elastic slopes: Part. I. Theoretical considerations. *Can. Geotech. J.* **20**, 47–54 (1983a).
30. Silvestri V. and Tabib C. Exact determination of gravity stresses in finite elastic slopes: Part. II. Applications. *Can. Geotech. J.* **20**, 55–60 (1983b).
31. Swolfs H. S. and Savage W. Z. Topographic modification of *in situ* stress in extensional and compressional tectonic environments. *Proc. Int. Sym. Rock Stress & Rock Stress Measurements*, pp. 89–98 (1986).